

BGK-Based Schemes for the Simulation of Compressible Flow

K. XU, C. KIM, L. MARTINELLI and A. JAMESON

*Department of Mechanical and Aerospace Engineering, Princeton University,
Princeton, New Jersey 08544, USA*

(Received 10 August 1995; Revised 21 December 1995; In final form 8 February 1996)

Following van Leer's MUSCL idea, a numerical scheme can be regarded as consisting of two key steps: a reconstruction step followed by a gas evolution step. We present a gas-kinetic method based on the collisional BGK model which provides an alternative to Riemann solvers for the gas evolution step. An advanced BGK-scheme is derived under quite general assumptions on the initial conditions. The new formulation uses interpolation of the characteristic variables in the reconstruction step and a BGK-type flow solver in the gas evolution step. The scheme satisfies both an entropy condition and a positivity condition, which guarantees a positive density and temperature at the cell interface during a complete time step. Numerical results for one-dimensional and two-dimensional test cases are presented to show the accuracy and robustness of the proposed approach.

Keywords: Characteristic reconstruction, BGK-type flow solver, compressible flows, entropy and positivity conditions

1. INTRODUCTION

Based largely on the mathematical foundation laid among others by Lax [16] and Godunov [6], many high resolution shock capturing schemes have been developed in the past twenty years. Most of them attempt to resolve wave interactions through upwind biasing of the discretization, while other methods explicitly introduce a numerical viscosity in just the amount needed to capture discontinuities [11]. Although great advances have been made in the area of spatial discretization, grid generation and solution strategies, the status of unsteady com-

pressible flow solvers is far from satisfactory for both structured and unstructured grids. Since the simulation of unsteady flows is emerging as an important area of practical interest, there is a compelling need for schemes with low dissipation and dispersion errors. The design principle should be guided by the "dynamics" of the "computational fluid" which should mimic, as closely as possible, those of a real fluid [28]. The simulation of highly compressible flow with strong shock waves and extreme expansion waves requires a numerical scheme which is capable of handling both flow features. BGK-type schemes mimic the real dynami-

cal process of the gas and could overcome many of the weaknesses of the traditional central difference and upwind methods. In particular, schemes of this class may provide a superior resolution of both shocks and expansion regions as well as contact discontinuities.

According to the MUSCL idea [32], a high resolution scheme usually consists of two parts, the reconstruction of the initial data and the dynamical evolution from the constructed data. These two stages can be regarded respectively as geometrical and dynamical correlations for the gas flow around an artificially defined cell boundary. Currently available techniques such as Total Variation Diminishing (TVD), Essentially Nonoscillation (ENO) and Local Extremum Diminishing (LED) [7, 8, 11] schemes, which are well understood for scalar conservation laws, can be used in the reconstruction stage for systems of equations. In the gas evolution stage, however, the solution is not necessarily a decreasing function of time and local extrema can be generated by nonlinear wave interactions.

The development of numerical schemes based on the gas-kinetic theory started in the 1970s with the beam scheme [29]. This scheme has been widely used in the astrophysical community and it is based on the collisionless Boltzmann equation. In the beam scheme, the left and right moving particles generated in each side from the equilibrium state are allowed to penetrate the opposite side through a cell interface giving rise to the numerical fluxes. In the 1980's, the beam scheme was re-invented, modified or extended by many authors, such as Reitz [26], Pullin [24], Deshpande [3] and Perthame [22]. Pullin was the first to use the complete error function to obtain the numerical fluxes: his scheme is named Equilibrium Flux Method (EFM). By applying the Courant-Isaacson-Reeves (CIR) upwind technique directly to the collisionless Boltzmann equation, Mandal and Deshpande derived a similar scheme, which is named Kinetic Flux Vector Splitting (KFVS) [21]. Perthame simplified these schemes by using a square or half dome function as the equilibrium gas distribution function. By combining the KFVS scheme with the multidimensional

upwinding techniques developed by several researchers at the University of Michigan and the von Karman Institute, Eppard and Grossman formulated several versions of first order multidimensional gas-kinetic schemes [5].

All above schemes are based on the *collisionless* Boltzmann equation, which does not account for the dynamical correlations between the left and right states. As pointed out by Macrossan [19], schemes of this kind have intrinsically large numerical viscosity and heat conductivity. In an effort to reduce the artificial viscosity, Xu and Prendergast in 1991 developed the Total Thermalized Transport (TTT) scheme [34], which is based on the physical assumption that the left and right moving beams collapse instantaneously at the cell interface to form an equilibrium state. The beam scheme and TTT scheme are two extreme limits describing the real particle motion. In order to model more accurately the real physical situation, a scheme called Partial Thermalized Transport (PTT), which is obtained by using a linear combination of the beam and the TTT scheme, was also developed. This hybrid scheme was found to behave nicely for shock tube simulations. At the same time, Macrossan and Oliver independently developed the so called Equilibrium Interface Method (EIM). EIM is similar to the TTT scheme and is derived using the same physical considerations [20]. A new scheme based on the TTT and the beam scheme has also been developed by the authors and applied to steady state airfoil calculations [36].

During the same period, new gas-kinetic schemes based on the collisional BGK model have been developed [23, 35, 36] to model the gas evolution process more precisely. Schemes of this class are named BGK-type schemes in order to distinguish them from other Boltzmann-type schemes based on the collisionless Boltzmann equation. BGK-type schemes make local use of the full integral solution of the BGK model. It is then possible to compute a time-dependent gas distribution function at the cell interface and to obtain the numerical fluxes. This approach, also, avoids the ambiguity of adding *ad hoc* models for particle collisions designed only to reduce the numerical viscosity which is intrinsic in

any of the Boltzmann-type schemes. Moreover, the BGK-type schemes give Navier-Stokes solutions which follow directly from the BGK model, and the gas relaxation from a nonequilibrium state to an equilibrium state is associated with an increase of entropy.

In this paper, we continue our previous work on the analysis of BGK-type schemes. By modifying some of the assumptions we develop a more general approximation of the equilibrium state around a cell boundary. This increases the robustness and accuracy of the BGK-type schemes. In Section 2, description of the basic finite volume gas-kinetic scheme in terms of the reconstruction and evolution ideas is presented. The section concludes with some useful and important remarks regarding the positivity and multidimensionality properties of the scheme. Finally, Section 3 presents a comprehensive summary of numerical results used to validate the current numerical approach.

2. FINITE VOLUME BGK-TYPE SCHEMES

The fundamental task in the construction of a finite-volume gas-kinetic scheme for compressible flow simulations is to evaluate the time-dependent gas distribution function f at a cell interface, from which the numerical fluxes can be computed. In a finite volume gas-kinetic scheme, the local solution of the gas-kinetic equation is used to compute the flux at the cell interface. Due to the intrinsic complexity of the collision integral in the full Boltzmann equation, simplified gas-kinetic models are usually used. In our approach the integral solution of the BGK model is used locally to compute the fluxes at the cell interface (see Fig.(1)). Hence, it replaces an approximate or exact Riemann solver. Since a single scalar distribution function f in the gas-kinetic theory includes all information about the macroscopic flow variables as well as their transport coefficients, the schemes in two-dimensions and three-dimensions can be constructed in a unified manner.

The BGK relaxation model [1] retains all the features of the Boltzmann equation which is asso-

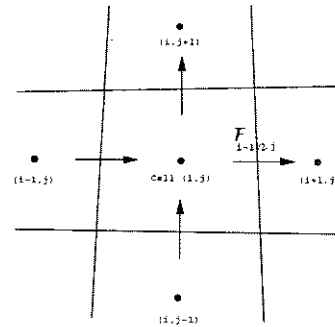


FIGURE 1 Interface fluxes by a finite volume gas-kinetic scheme.

ciated with the free molecular motion and describes approximately, in a mean-statistical fashion, the molecular collisions. The collisional term in the BGK model is the simplest of all possible formulations which reflect the nature of the particle collision phenomenon. Since in the continuum regime the behavior of the fluid depends very little on the nature of individual particles, the most important properties are: *conservation*, *symmetry* and *dissipation*. The BGK model satisfies all these requirements [17].

A numerical scheme based on the BGK model is equivalent to a scheme which approximates the Navier-Stokes equations [35, 36]. Earlier versions of the BGK-type schemes were based on the assumptions of a discontinuous nonequilibrium distribution f_0 and a continuous equilibrium state g across each cell interface at the beginning of each time step. Although these earlier schemes were found to give good results for a number of standard test cases, these assumptions can be still modified to improve the accuracy and reliability of the schemes for complex flows. In this paper we introduce a scheme which allows a slope discontinuity in the equilibrium state g , and also uses characteristic variables for the reconstruction.

2.1. Reconstruction Stage

Following van Leer's MUSCL idea, the present class of numerical scheme is composed of an initial reconstruction stage followed by a dynamical evol-

ution stage. At the beginning of each time step $t = 0$, cell averaged mass, momentum and energy densities are given. For a higher order scheme, interpolation techniques must be used to capture the subcell structure. Simple polynomials usually generate spurious oscillations if large gradients in the data are present. The most successful interpolation techniques known so far are based either on the TVD, ENO or LED principles [7, 8, 11]. These interpolation techniques can be applied to the conservative, characteristic or primitive flow variables. For example, some recent upwind schemes use characteristic variables in the reconstruction stage [8, 12, 30]. Unfortunately, depending on the particular test case, the numerical results may be sensitive to the particular set of variables used in the reconstruction step. In earlier BGK-type schemes, the reconstruction has been applied directly to the conservative variables. In this work, we try to take advantage of the smoothness property of the characteristic variables by using this particular set in the reconstruction step.

Let $x_j = jh$ ($j = 0, 1, 2, \dots$) be a uniform mesh and h the mesh size. Let $x_{j+1/2} = (j + 1/2)h$ be the interface between cells j and $j + 1$. The cell averaged value is denoted by U_j , and its interpolated value in cell j is $\bar{U}_j(x)$, with two pointwise values $\bar{U}_j(x_{j+1/2})$ and $\bar{U}_j(x_{j-1/2})$ at the locations $x_{j+1/2}$ and $x_{j-1/2}$. To second-order accuracy, the interpolated value in the j -th cell can be written as

$$\bar{U}_j(x) = U_j + L(U_{j-1}, \dots, U_{j+1})(x - x_j)$$

for

$$x_{j-1/2} \leq x \leq x_{j+1/2},$$

where l is an integer and $2l + 1$ is the extent of the stencil in the reconstruction process, and L is an interpolating function. For example, the second-order TVD and LED schemes have $l = 1$, while second-order ENO scheme has $l = 2$.

For higher order (more than second-order) reconstructions, the interpolating function may be defined recursively. In any case, the value $\bar{U}_j(x_j)$ at the cell center is not necessarily equal to the cell averaged value U_j .

Reconstruction using Characteristic Variables

Let j be a fixed cell with cell averaged mass ρ_j , momentum P_j and energy ε_j . The conservative variables are transformed to the primitive variables

$$V_j = (\rho_j, u_j, p_j)^T,$$

where u_j is the velocity and p_j is the pressure. The sound speed is $c_j = \sqrt{\gamma p_j / \rho_j}$. For cell j , we need three-point stencils for the reconstruction, for which $-1 \leq l \leq 1$. Set the characteristic variables in neighboring cell ($j + l$) as

$$W_l = \hat{L} V_{j+l} = \begin{pmatrix} -[\rho_j / (2c_j)] u_{j+l} + [1 / (2c_j^2)] p_{j+l} \\ \rho_{j+l} - [1 / c_j^2] p_{j+l} \\ [\rho_j / (2c_j)] u_{j+l} + [1 / (2c_j^2)] p_{j+l} \end{pmatrix},$$

where \hat{L} is the matrix of left eigenvectors at the state V_j for the Euler equations. For each component of the characteristic variables, we get $s_+ = (w_1 - w_0)/h$ and $s_- = (w_0 - w_{-1})/h$ as the slopes across the cell interface, and apply the MUSCL limiter

$$L(u, v) = S(u, v) \min \left(\frac{1}{2} |u + v|, 2|u|, 2|v| \right)$$

to s_+ and s_- to get the limited slope L . Then, for each component of the characteristic variable in cell j , we have

$$w_0(x_{j-1/2}) = w_0 - \frac{1}{2} h L(s_+, s_-)$$

and

$$w_0(x_{j+1/2}) = w_0 + \frac{1}{2} h L(s_+, s_-).$$

Once the interpolated value is obtained for each characteristic component, the distributions of the primitive variables in each cell at $x_{j-1/2}$ and $x_{j+1/2}$ can be found from the relation

$$V = \hat{R} W,$$

where the matrix \hat{R} is

$$\hat{R} = \begin{pmatrix} 1 & 1 & 1 \\ -c_j/\rho_j & 0 & c_j/\rho_j \\ c_j^2 & 0 & c_j^2 \end{pmatrix}.$$

Finally, the conservative variables

$$(\bar{\rho}_j(x_{j-1/2}), \bar{P}_j(x_{j-1/2}), \bar{e}_j(x_{j-1/2}))$$

and

$$(\bar{\rho}_j(x_{j+1/2}), \bar{P}_j(x_{j+1/2}), \bar{e}_j(x_{j+1/2}))$$

are obtained by the reverse transformation.

2.2. The BGK-Type Flow Solver

The BGK model in one-dimension can be written as

$$f_t + uf_x = \frac{g-f}{\tau}, \quad (1)$$

where f is the real gas distribution function and g is the equilibrium state approached by f . Both f and g are functions of space x , time t , particle velocity u and internal degrees of freedom ξ . The particle collision time τ depends on the local macroscopic flow variables, such as temperature and density. The equilibrium state is usually assumed to be a Maxwellian, with the formulation

$$g = \rho \left(\frac{\lambda}{\pi} \right)^{(K+1)/2} e^{-\lambda((u-U)^2 + \xi^2)},$$

where ρ is the density and U is the macroscopic velocity. In the one-dimensional case, when the particle motion in y and z direction is included as internal degrees of freedom [15], the total number of degrees of freedom K is equal to $(5-3\gamma)/(\gamma-1)+2$. The relations between mass ρ , momentum P and energy densities ε with the distribution function f are

$$\begin{pmatrix} \rho \\ P \\ \varepsilon \end{pmatrix} = \int \psi_\alpha f d\Xi, \quad \alpha = 1, 2, 3, \quad (2)$$

where ψ_α is the vector of moments

$$\psi_\alpha = \left(1, u, \frac{1}{2}(u^2 + \xi^2) \right)^T,$$

and $d\Xi = dud\xi$ is the volume element in the phase space. Since mass, momentum and energy are conserved during particle collisions, f and g must satisfy the conservation constraint

$$\int (g-f) \psi_\alpha d\Xi = 0, \quad \alpha = 1, 2, 3 \quad (3)$$

at any point in space and time.

For a local equilibrium state with $f = g$, the Euler equations can be obtained by taking the moments of ψ_α to Eq.(1). This yields

$$\int \begin{pmatrix} 1 \\ u \\ \frac{1}{2}(u^2 + \xi^2) \end{pmatrix} (g_t + ug_x) dud\xi = 0,$$

and the corresponding Euler equations are

$$\begin{pmatrix} \rho \\ \rho U \\ \frac{1}{2}\rho(U^2 + \frac{K+1}{2\lambda}) \end{pmatrix}_t + \begin{pmatrix} \rho U \\ \rho U^2 + \frac{p}{2\lambda} \\ \frac{1}{2}\rho(U^3 + \frac{(K+3)U}{2\lambda}) \end{pmatrix}_x = 0,$$

where the pressure term is $p = \rho/2\lambda$.

On the other hand, to the first order of τ , the Chapman-Enskog expansion [15] gives $f = g - \tau(g_t + ug_x)$. Taking moments of ψ_α again to the BGK equation with the new f , we get

$$\begin{aligned} & \int \begin{pmatrix} 1 \\ u \\ \frac{1}{2}(u^2 + \xi^2) \end{pmatrix} (g_t + ug_x) dud\xi \\ &= \tau \int \begin{pmatrix} 1 \\ u \\ \frac{1}{2}(u^2 + \xi^2) \end{pmatrix} (g_{tt} + 2ug_{xt} + u^2 g_{xx}) dud\xi. \end{aligned}$$

After integrating out all the moments, the Navier-Stokes equations with a dynamic viscous coefficient

$\eta = \tau p$ can be expressed as

$$\begin{aligned} & \left(\begin{array}{c} \rho \\ \rho U \\ \frac{1}{2} \rho (U^2 + \frac{K+1}{2\lambda}) \end{array} \right)_t + \left(\begin{array}{c} \rho U \\ \rho U^2 + \frac{\rho}{2\lambda} \\ \frac{1}{2} \rho (U^3 + \frac{(K+3)U}{2\lambda}) \end{array} \right)_x \\ &= \tau \left(\begin{array}{c} 0 \\ \frac{2K}{K+1} \frac{\rho}{2\lambda} U_x \\ \frac{K+3}{4} \frac{\rho}{2\lambda} (\frac{1}{\lambda})_x + \frac{2K}{K+1} \frac{\rho}{2\lambda} U U_x \end{array} \right)_x. \end{aligned}$$

The general solution of f at the cell interface $x_{j+1/2}$ and time t is

$$\begin{aligned} f(x_{j+1/2}, t, u, \xi) &= \frac{1}{\tau} \int_0^t g(x', t', u, \xi) e^{-(t-t')/\tau} dt' \\ &+ e^{-t/\tau} f_0(x_{j+1/2} - ut), \end{aligned} \quad (4)$$

where $x' = x_{j+1/2} - u(t-t')$ is the trajectory of a particle motion and f_0 is the initial nonequilibrium distribution function f at the beginning of each time step ($t=0$) [15]. The two values g and f_0 must be specified in Eq.(4) in order to obtain the desired solution for f .

Generally, f_0 and g around the cell interface $x_{j+1/2}$ are assumed to be

$$f_0 = \begin{cases} g^l(1 + a^l(x - x_{j+1/2})), & x \leq x_{j+1/2} \\ g^r(1 + a^r(x - x_{j+1/2})), & x \geq x_{j+1/2} \end{cases} \quad (5)$$

and

$$\begin{aligned} g &= g_0(1 + (1 - H[x - x_{j+1/2}])\bar{a}^l(x - x_{j+1/2}) \\ &+ H[x - x_{j+1/2}]\bar{a}^r(x - x_{j+1/2}) + \bar{A}t), \end{aligned} \quad (6)$$

where g^l, g^r and g_0 are local Maxwellian distribution functions, which are located, respectively, to the left, to the right and in the middle of a cell interface. $a^l, a^r, \bar{a}^l, \bar{a}^r$ are slopes. $H[x]$ is the Heaviside function defined as

$$H[x] = \begin{cases} 0, & x < 0 \\ 1, & x \geq 0 \end{cases}$$

Notice that in the expansion of g , the possibility of discontinuous slopes has been retained. This is different from our previous approaches [23,35,36,13]. The dependence of a^l, a^r, \dots, \bar{A} on the particle velocities is obtained from the Taylor expansion of a Maxwellian and these quantities have the form

$$a^l = a_1^l + a_2^l u + a_3^l \frac{1}{2}(u^2 + \xi^2) = a_\alpha^l \psi_\alpha,$$

$$a^r = a_1^r + a_2^r u + a_3^r \frac{1}{2}(u^2 + \xi^2) = a_\alpha^r \psi_\alpha,$$

$$\bar{a}^r = \bar{a}_1^r + \bar{a}_2^r u + \bar{a}_3^r \frac{1}{2}(u^2 + \xi^2) = \bar{a}_\alpha^r \psi_\alpha,$$

$$\bar{a}^l = \bar{a}_1^l + \bar{a}_2^l u + \bar{a}_3^l \frac{1}{2}(u^2 + \xi^2) = \bar{a}_\alpha^l \psi_\alpha,$$

$$\bar{A} = \bar{A}_1 + \bar{A}_2 u + \bar{A}_3 \frac{1}{2}(u^2 + \xi^2) = \bar{A}_\alpha \psi_\alpha,$$

where all coefficients of $a_1^l, a_2^l, \dots, \bar{A}_3$ are local constants. The idea of interpolating f_0 separately in the regions $x \leq x_{j+1/2}$ and $x \geq x_{j+1/2}$ originates from the following physical consideration: for a non-equilibrium gas flow, since the cell size is usually much larger than the thickness of a discontinuity, the physical quantities can change dramatically in space. For example, across a shock front, the upstream and downstream gas distribution functions could be two different Maxwellians. Therefore, we need a splitting of f_0 to capture this physical situation.

In the reconstruction stage described in Section (2.1), we have obtained $\bar{\rho}_j(x)$, $\bar{P}_j(x)$ and $\bar{e}_j(x)$ in each cell $x_{j-1/2} \leq x \leq x_{j+1/2}$. At the cell interface $x_{j+1/2}$, the left and right side pointwise values are

$$(\bar{\rho}_j(x_{j+1/2}), \bar{\rho}_{j+1}(x_{j+1/2})),$$

$$(\bar{P}_j(x_{j+1/2}), \bar{P}_{j+1}(x_{j+1/2})),$$

$$(\bar{e}_j(x_{j+1/2}), \bar{e}_{j+1}(x_{j+1/2})).$$

By using the relation between the gas distribution function f_0 and the macroscopic variables (Eq.(2)),

we get

$$\begin{aligned}
 \int g^l \psi_\alpha d\mathbf{u} d\xi &= \begin{pmatrix} \bar{\rho}_j(x_{j+1/2}) \\ \bar{P}_j(x_{j+1/2}) \\ \bar{\varepsilon}_j(x_{j+1/2}) \end{pmatrix}; \\
 \int g^l a^l \psi_\alpha d\mathbf{u} d\xi &= \begin{pmatrix} \frac{\bar{\rho}_j(x_{j+1/2}) - \bar{\rho}_j(x_j)}{\Delta x^-} \\ \frac{\bar{P}_j(x_{j+1/2}) - \bar{P}_j(x_j)}{\Delta x^-} \\ \frac{\bar{\varepsilon}_j(x_{j+1/2}) - \bar{\varepsilon}_j(x_j)}{\Delta x^-} \end{pmatrix} \\
 \int g^r \psi_\alpha d\mathbf{u} d\xi &= \begin{pmatrix} \bar{\rho}_{j+1}(x_{j+1/2}) \\ \bar{P}_{j+1}(x_{j+1/2}) \\ \bar{\varepsilon}_{j+1}(x_{j+1/2}) \end{pmatrix}; \\
 \int g^r a^r \psi_\alpha d\mathbf{u} d\xi &= \begin{pmatrix} \frac{\bar{\rho}_{j+1}(x_{j+1}) - \bar{\rho}_{j+1}(x_{j+1/2})}{\Delta x^+} \\ \frac{\bar{P}_{j+1}(x_{j+1}) - \bar{P}_{j+1}(x_{j+1/2})}{\Delta x^+} \\ \frac{\bar{\varepsilon}_{j+1}(x_{j+1}) - \bar{\varepsilon}_{j+1}(x_{j+1/2})}{\Delta x^+} \end{pmatrix}, \quad (7)
 \end{aligned}$$

where $\Delta x^- = x_{j+1/2} - x_j$ and $\Delta x^+ = x_{j+1} - x_{j+1/2}$.
With the definition of the Maxwellian distributions

$$\begin{aligned}
 g^l &= \rho^l \left(\frac{\lambda^l}{\pi} \right)^{\frac{K+1}{2}} e^{-\lambda^l((u-U)^2 + \xi^2)}, \\
 g^r &= \rho^r \left(\frac{\lambda^r}{\pi} \right)^{\frac{K+1}{2}} e^{-\lambda^r((u-U)^2 + \xi^2)},
 \end{aligned}$$

and from Eq.(7), all the parameters in g^l and g^r can be uniquely determined from

$$M_{\alpha\beta}^r = \begin{pmatrix} 1 & U^r & \frac{1}{2}(U^{r2} + \frac{K+1}{2\lambda^r}) \\ U^r & U^{r2} + \frac{1}{2\lambda^r} & \frac{1}{2}(U^{r3} + \frac{(K+3)U^r}{2\lambda^r}) \\ \frac{1}{2}(U^{r2} + \frac{K+1}{2\lambda^r}) & \frac{1}{2}(U^{r3} + \frac{(K+3)U^r}{2\lambda^r}) & \frac{1}{4}(U^{r4} + \frac{(K+3)U^{r2}}{\lambda^r} + \frac{(K^2+4K+3)}{4\lambda^{r2}}) \end{pmatrix}$$

$$\begin{pmatrix} \rho^l \\ U^l \\ \lambda^l \end{pmatrix} = \begin{pmatrix} \bar{\rho}_j(x_{j+1/2}) \\ \bar{P}_j(x_{j+1/2})/\bar{\rho}_j(x_{j+1/2}) \\ \frac{(K+1)\bar{\rho}_j(x_{j+1/2})}{4(\bar{\varepsilon}_j(x_{j+1/2}) - \frac{1}{2}\bar{P}_j^2(x_{j+1/2})/\bar{\rho}_j(x_{j+1/2}))} \end{pmatrix}$$

and

$$\begin{pmatrix} \rho^r \\ U^r \\ \lambda^r \end{pmatrix} = \begin{pmatrix} \bar{\rho}_{j+1}(x_{j+1/2}) \\ \bar{P}_{j+1}(x_{j+1/2})/\bar{\rho}_{j+1}(x_{j+1/2}) \\ \frac{(K+1)\bar{\rho}_{j+1}(x_{j+1/2})}{4(\bar{\varepsilon}_{j+1}(x_{j+1/2}) - \frac{1}{2}\bar{P}_{j+1}^2(x_{j+1/2})/\bar{\rho}_{j+1}(x_{j+1/2}))} \end{pmatrix}$$

Once g^r is obtained from the above equations, the slope of a^r can be computed:

$$\begin{aligned}
 &\begin{pmatrix} \frac{\bar{\rho}_{j+1}(x_{j+1}) - \bar{\rho}_{j+1}(x_{j+1/2})}{\rho^r \Delta x^+} \\ \frac{\bar{P}_{j+1}(x_{j+1}) - \bar{P}_{j+1}(x_{j+1/2})}{\rho^r \Delta x^+} \\ \frac{\bar{\varepsilon}_{j+1}(x_{j+1}) - \bar{\varepsilon}_{j+1}(x_{j+1/2})}{\rho^r \Delta x^+} \end{pmatrix} \\
 &= \begin{pmatrix} \Delta \rho^r \\ \Delta P^r \\ \Delta \varepsilon^r \end{pmatrix} = M_{\alpha\beta}^r \begin{pmatrix} a_1^r \\ a_2^r \\ a_3^r \end{pmatrix} = M_{\alpha\beta}^r a_\beta^r, \quad (8)
 \end{aligned}$$

where the matrix $M_{\alpha\beta}^r = 1/\rho^r \int g^r \psi_\alpha \psi_\beta d\Xi$ is

From Eq. (8), $(a_1^r, a_2^r, a_3^r)^T$ can be readily obtained by observing that $M_{\alpha\beta}^r$ is a symmetric matrix. Thus, we obtain

$$\begin{aligned} a_3^r &= \frac{4\lambda^{r2}}{K+1}(\mathcal{B} - 2U^r\mathcal{A}), \\ a_2^r &= 2\lambda^r\left(\mathcal{A} - \frac{a_3^r U^r}{2\lambda^r}\right), \\ a_1^r &= \Delta\rho^r - a_2^r U^r - a_3^r\left(\frac{U^{r2}}{2} + \frac{K+1}{4\lambda^r}\right), \end{aligned} \quad (9)$$

where

$$\begin{aligned} \mathcal{A} &= \Delta P^r - U^r \Delta\rho^r, \\ \mathcal{B} &= 2\Delta\varepsilon^r - \left(U^{r2} + \frac{K+1}{2\lambda^r}\right)\Delta\rho^r. \end{aligned}$$

Since the matrix $M_{\alpha\beta}^l = 1/\rho^l \int g^l \psi_\alpha \psi_\beta d\Xi$ has the same structure as $M_{\alpha\beta}^r$, $(a_1^l, a_2^l, a_3^l)^T$ can be obtained using a similar procedure.

After determining f_0 , the corresponding values of ρ_0 , U_0 and λ_0 in g_0 with

$$g_0 = \rho_0 \left(\frac{\lambda_0}{\pi}\right)^{(k+1)/2} e^{-\lambda_0((u-U_0)^2 + \xi^2)}$$

can be determined as follows. Taking the limit $t \rightarrow 0$ in Eq. (4) and substituting its solution into Eq. (3), the conservation constraint at $(x = x_{j+1/2}, t = 0)$ gives

$$\begin{aligned} \int g_0 \psi_\alpha d\Xi &= \int_{u>0} \int g^l \psi_\alpha d\Xi \\ &+ \int_{u<0} \int g^r \psi_\alpha d\Xi, \alpha = 1, 2, 3 \end{aligned} \quad (10)$$

This equation validates the basic idea of the TTT scheme. Since λ_0 can be found from ρ_0 , U_0 and ε_0

through the relation

$$\lambda_0 = (K+1)\rho_0 \left/ \left(4\left(\varepsilon_0 - \frac{1}{2}\rho_0 U_0^2 \right) \right) \right.,$$

We only need to know $(\rho_0, U_0, \varepsilon_0)^T$, which can be expressed as moments of g^l and g^r . By introducing the notation

$$\begin{aligned} \rho^l \langle \dots \rangle_{>0} &= \int_{u>0} (\dots) g^l d\Xi, \\ \rho^l \langle \dots \rangle_{<0} &= \int_{u<0} (\dots) g^r d\Xi, \end{aligned}$$

from Eq. (10) one obtains

$$\begin{pmatrix} \rho_0 \\ \rho_0 U_0 \\ \varepsilon_0 \end{pmatrix} = \begin{pmatrix} \rho^l \langle u^0 \rangle_{>0} + \rho^r \langle u^0 \rangle_{<0} \\ \rho^l \langle u^1 \rangle_{>0} + \rho^r \langle u^1 \rangle_{<0} \\ 1/2(\rho^l \langle u^2 + \xi^2 \rangle_{>0} + \rho^r \langle u^2 + \xi^2 \rangle_{<0}) \end{pmatrix}$$

A detailed derivation can be found in the Appendix B. Then, \bar{a}^l and \bar{a}^r of g in Eq. (6) can be obtained through the relation of

$$\begin{pmatrix} \frac{\bar{\rho}_{j+1}(x_{j+1}) - \rho_0}{\rho_0 \Delta x^+} \\ \frac{P_{j+1}(x_{j+1}) - P_0}{\rho_0 \Delta x^+} \\ \frac{\bar{\varepsilon}_{j+1}(x_{j+1}) - \varepsilon_0}{\rho_0 \Delta x^+} \end{pmatrix} = \bar{M}_{\alpha\beta}^0 \begin{pmatrix} \bar{a}_1^r \\ \bar{a}_2^r \\ \bar{a}_3^r \end{pmatrix} = \bar{M}_{\alpha\beta}^0 \bar{a}_\beta^r,$$

and

$$\begin{pmatrix} \frac{\rho_0 - \bar{\rho}_j(x_j)}{\rho_0 \Delta x^-} \\ \frac{P_0 - \bar{P}_j(x_j)}{\rho_0 \Delta x^-} \\ \frac{\varepsilon_0 - \bar{\varepsilon}_j(x_j)}{\rho_0 \Delta x^-} \end{pmatrix} = \bar{M}_{\alpha\beta}^0 \begin{pmatrix} \bar{a}_1^l \\ \bar{a}_2^l \\ \bar{a}_3^l \end{pmatrix} = \bar{M}_{\alpha\beta}^0 \bar{a}_\beta^l.$$

The matrix $\bar{M}_{\alpha\beta}^0 = 1/\rho_0 \int g_0 \psi_\alpha \psi_\beta d\Xi$ has the same structure as $M_{\alpha\beta}^r$, which is

$$\bar{M}_{\alpha\beta}^0 = \begin{pmatrix} 1 & U_0 & \frac{1}{2}\left(U_0^2 + \frac{K+1}{2\lambda_0}\right) \\ U_0 & U_0^2 + \frac{1}{2\lambda_0} & \frac{1}{2}\left(U_0^3 + \frac{(K+3)U_0}{2\lambda_0}\right) \\ \frac{1}{2}\left(U_0^2 + \frac{K+1}{2\lambda_0}\right) & \frac{1}{2}\left(U_0^3 + \frac{(K+3)U_0}{2\lambda_0}\right) & \frac{1}{4}\left(U_0^4 + \frac{(K+3)U_0^2}{\lambda_0} + \frac{(K^2+4K+3)}{4\lambda_0^2}\right) \end{pmatrix}.$$

Therefore, $(\bar{a}_1^r, \bar{a}_2^r, \bar{a}_3^r)^T$ and $(\bar{a}_1^l, \bar{a}_2^l, \bar{a}_3^l)^T$ can be found following the procedure used to obtain Eq.(9).

Up to this point, we have found two half-Maxwellian and one whole Maxwellian distribution function at the cell interface $x_{j+1/2}$ and they represent the nonequilibrium state f_0 and equilibrium state g_0 . All the slopes in the expression of a^l , a^r in f_0 and \bar{a}^l , \bar{a}^r in g are determined from the slopes of macroscopic variables. Notice that the construction of two slopes for g proposed in this paper gives more freedom to describe complicated flow situations. Notice, also, that for Navier-Stokes solutions, the slopes of \bar{a}^l and \bar{a}^r represent the viscosity and heat conduction effects [36].

After substituting Eq. (5) and Eq. (6) into Eq. (4), the final gas distribution function at a cell interface is expressed as

$$\begin{aligned} f(x_{j+1/2}, t, u, \xi) &= (1 - e^{-t/\tau})g_0 \\ &+ \left(\tau(-1 + e^{-t/\tau}) + te^{-t/\tau} \right) (\bar{a}^l H[u] \\ &+ \bar{a}^r (1 - H[u]))ug_0 \\ &+ \tau(t/\tau - 1 + e^{-t/\tau})\bar{A}g_0 \\ &+ e^{-t/\tau}((1 - uta^l)H[u]g^l \\ &+ (1 - uta^r)(1 - H[u])g^r). \end{aligned} \quad (12)$$

The only unknown term in the above equation is \bar{A} . Since both f (Eq.(12)) and g (Eq.(6)) contain \bar{A} , after applying the conservation constraint of Eq.(3) at $x_{j+1/2}$ and integrating it over the whole time step T ,

we get

$$\int_0^T \int (g - f) \psi_\alpha dt d\Xi = 0,$$

which gives

$$\begin{aligned} \bar{M}_{\alpha\beta}^0 \bar{A}_\beta &= \frac{1}{\rho_0} \int [\gamma_1 g_0 + \gamma_2 u (\bar{a}^l H[u] \\ &+ \bar{a}^r (1 - H[u]))g_0 \\ &+ \gamma_3 (H[u]g^l + (1 - H[u])g^r) \\ &+ \gamma_4 u (a^l H[u]g^l + a^r (1 - H[u])g^r)] \psi_\alpha d\Xi, \end{aligned} \quad (13)$$

where

$$\begin{aligned} \gamma_0 &= T - \tau(1 - e^{-T/\tau}), \\ \gamma_1 &= -(1 - e^{-T/\tau})/\gamma_0, \\ \gamma_2 &= (-T + 2\tau(1 - e^{-T/\tau}) - Te^{-T/\tau})/\gamma_0, \\ \gamma_3 &= (1 - e^{-T/\tau})/\gamma_0, \\ \gamma_4 &= (Te^{-T/\tau} - \tau(1 - e^{-T/\tau}))/\gamma_0. \end{aligned}$$

All moments of the Maxwellian on the right hand side of Eq.(13) can be found in Appendix B and the above equation can be solved for $(\bar{A}_1, \bar{A}_2, \bar{A}_3)^T$.

Finally, the time-dependent numerical fluxes in the x -direction across the cell interface can be computed as

$$\begin{pmatrix} \mathcal{F}_\rho \\ \mathcal{F}_p \\ \mathcal{F}_\varepsilon \end{pmatrix}_{j+1/2} = \int u \begin{pmatrix} 1 \\ u \\ \frac{1}{2}(u^2 + \xi^2) \end{pmatrix} f(x_{j+1/2}, t, u, \xi) d\Xi, \quad (14)$$

where $f(x_{j+1/2}, t, u, \xi)$ is given in Eq. (12). By integrating the above equation to the whole time step, we get the total mass, momentum and energy transport. These fluxes satisfy the consistency condition of $\mathcal{F}(U, U) = \mathcal{F}(U)$ for a homogeneous uniform flow, where $\mathcal{F}(U)$ are the corresponding Euler fluxes.

2.3. Numerical Analysis

One of the obvious improvement in this new version of the BGK-type schemes is that we have relaxed the original assumption of a single continuous slope for the equilibrium state g across a cell interface, and generalized the initial conditions for the gas-evolution model. This significantly increases the robustness of the BGK-type schemes. The computational cost of the new scheme is slightly higher than that of the previous schemes due to additional computations required by the two slopes in Eq.(6). Nevertheless, in our experience, the CPU time required by the current approach is comparable to that of a second-order extension of Roe's approximate Riemann solver with entropy fixes.

Remark(1) The construction of g_0 in term of g^l and g^r is a natural consequence of the solution of the BGK model, which physically validates the assumptions of the TTT scheme [34]. This stage is similar to the use of Roe's average to construct a common state at a cell boundary. However, in gas-kinetic theory, the equilibrium state is formed between the left and right beams due to particle collisions. In a previous paper [36], we have proved that g_0 has larger entropy than the original nonequilibrium state f_0 . The point that should be emphasized here is that the density and temperature in Eq. (11), corresponding to the equilibrium distribution g_0 , could possibly be outside the range determined by the left and right states. For example, the following inequalities could be true under some conditions:

$$\rho_0 > \max(\rho^l, \rho^r); \lambda_0 < \min(\lambda^l, \lambda^r).$$

One example is that of two shocks collapsing to form a stronger shock around the cell interface with larger density and higher temperature. Or, two rarefaction waves at the left and right sides of a cell interface which create a lower density region at the center.

Thus, in the dynamical stage, the maximum or minimum of density and temperature could be increased or decreased, and our construction of g_0 is capable of capturing these phenomena.

Remark(2) As derived in Section(2.2), the BGK model converges to the Navier-Stokes equations in its second-order approximation. Also, as we have shown in [36], the viscous fluxes are related to the linear slope of g at the cell interface, and the BGK-type schemes give the Navier-Stokes equations with dynamical viscosity $\eta = \tau p$ and Prandtl number $Pr = 1$ in smooth regions. The smooth regions could include the boundary or shock layers if the grid size is small enough to resolve these layers [35]. For Euler calculations, the final gas distribution function can be much simplified [37].

Remark(3) In contrast to the Riemann solver, the BGK-type schemes provide an advanced gas evolution model. From Eq.(11), we know that g_0 has positive density and temperature if g^l and g^r obtained in the reconstruction stage are physical states with positive density and temperature. Then, $g_0 > 0$ is satisfied, which means that all particles have positive probability. If we ignore all slopes in the BGK-type schemes, the distribution function f at the cell interface can be written as

$$f(x_{j+1/2}, t) = (1 - e^{-t/\tau})g_0 + e^{-t/\tau}f_0.$$

Since $g_0 > 0, f_0 > 0$ and $e^{-t/\tau} < 1$, f is strictly positive with $f > 0$. Therefore, f has positive density and temperature due to the following relations

$$\int f d\Xi > 0; \quad \int u^2 f d\Xi - \frac{(\int u f d\Xi)^2}{\int f d\Xi} > 0.$$

This is a positivity condition for the BGK-type schemes. Roe's approximate Riemann solver cannot guarantee that the solutions of the flow variables at the cell interface satisfy a positivity condition [4, 27]. Thus, it appears that the BGK-type schemes provide more realistic solutions.

Remark(4) From gas-kinetic theory, the collision time should depend on macroscopic flow variables, such as density and temperature. For BGK-type numerical schemes, the collision time τ is composed

of two parts

$$\tau = C_1 \frac{\sqrt{\lambda_0}}{\rho_0} + C_2 T \frac{|\rho^l/\lambda^l - \rho^r/\lambda^r|}{|\rho^l/\lambda^l + \rho^r/\lambda^r|},$$

where T is the time step, C_1 is chosen according to the Reynolds number and C_2 is of order 1 for most cases. The two terms in the collision time are equivalent to a physical and a numerical viscosity. In most cases, the mesh size is not small enough to resolve the discontinuities. Therefore, we have to regard the thickness of the discontinuity as being, at least, as large as a few cell sizes, and additional viscosity is necessary to satisfy this requirement. For all Euler test cases, the results are not very sensitive to the values of C_1 and C_2 , and C_1 is usually of the order of 10^{-2} if $\Delta x = 1$. The additional term in the collision time can be regarded as a limiter imposed in the time domain in the dynamical stage, which is similar to the conventional limiter imposed in the space domain during the reconstruction stage when the order of space accuracy is more than first-order. Therefore, the concept of limiter should be extended to both space and time if a numerical scheme couples them and has uniformly high order accuracy. One advantage of the BGK-type scheme is that an explicit expression for the total viscosity can be computed. This avoids the ambiguity of implicit viscosities present in most upwind schemes.

Remark(5) In an earlier paper [36], we have illustrated the entropy condition for BGK-type schemes. Here one point should be emphasized: the BGK model itself satisfies the entropy condition (dissipative property) [15]. This is in contrast with the Euler equations, where the entropy condition has to be added. Thus, if a scheme uses the BGK model correctly, there would not be any mechanism to create unphysical phenomena such as expansion shocks.

Remark(6) For two dimensional flow, the linearized form of the Navier-Stokes equations is

$$W_t + AW_x + BW_y = S.$$

It is well known that the difficulties in the development of multidimensional upwind schemes for the Navier-Stokes equations is due to the fact that the matrices A and B do not commute: $[A, B] \equiv AB - BA \neq 0$. Physically, it means that an infinite number of waves are present in the flow. Therefore, the necessity of wave modeling follows.

However, for the BGK model

$$f_t + uf_x + vf_y = (g - f)/\tau,$$

the particle velocities are independent variables and this difficulty is eliminated.

Thus, in the BGK-type schemes we can consider all particles in all directions. Theoretically, there is not any obvious obstacle to get a multidimensional BGK-type scheme provided that a truly "multi-dimensional" initial reconstruction is developed.

Remarks(7) If higher order terms are included in the expansion of f_0 and g , i.e.

$$g = g_0(1 + \bar{a}x + \bar{b}x^2 + \bar{B}xt + \bar{A}t + \bar{C}t^2).$$

the BGK model can be still solved numerically using the generalized conservation constraints

$$\frac{\partial^{m+n}}{\partial x^n \partial t^m} \int (f - g) \psi_z d\Xi = 0.$$

The higher order BGK schemes will be developed for the aeroacoustic problems in the near future.

3. NUMERICAL EXPERIMENTS

The new numerical scheme has been applied to several test cases ranging from a simple advection-diffusion equation to hypersonic flow computations. Unless otherwise stated, in all of the numerical examples reported, $\gamma = 1.4$ and the MUSCL limiter is used.

Case (1) Advection-Diffusion Equation

A previous study of the BGK-type flux function for the advection equation has shown an interesting

algorithmic structure [13]. In particular, it turns out that the numerical fluxes can be regarded as a non-linear time-dependent combination of the Lax-Wendroff type schemes with the Kinetic Flux Vector Splitting. Details of the numerical discretization of the BGK-type scheme for the linear advection-diffusion equation are presented in Appendix A. In order to compare the results obtained with our BGK-type scheme with others in the literature, ENO interpolation is employed in the reconstruction stage. Figure (2)–Figure (3) show the computed results of a decaying sinusoidal wave after one period ($t = 2.0$) corresponding to Reynolds numbers $Re (\equiv cL/\nu)$ of 400, 2000, respectively. The computations use 40 cells, and a CFL number of 0.1. A comparison with the results of Chiu and Zhong [2] reveals that our results obtained with higher order (more than second order) are almost indistinguishable from those reported in the literature. However, first-order and second-order results obtained with the BGK-type schemes are much better. A grid refinement study using a second-order MUSCL limiter also verifies excellent convergence characteristics of the scheme. Figure (4)–Figure (5) show that the numerical results obtained with more than 80 cells practically collapse onto the exact solution.

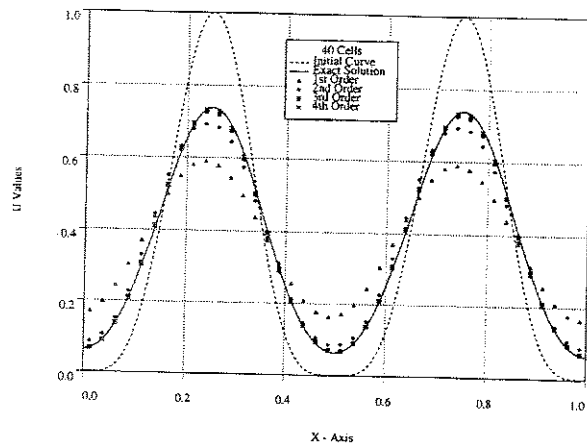


FIGURE 2 Advection-Diffusion Case with ENO Limiter and BGK Solver ($Re = 400$).

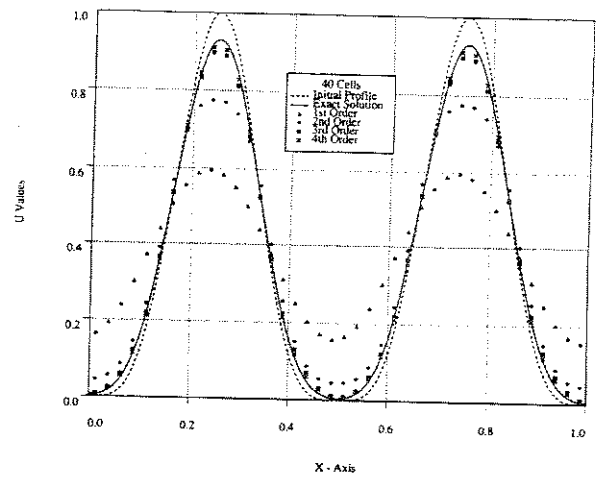


FIGURE 3 Advection-Diffusion Case with ENO Limiter and BGK solver ($Re = 2000$).

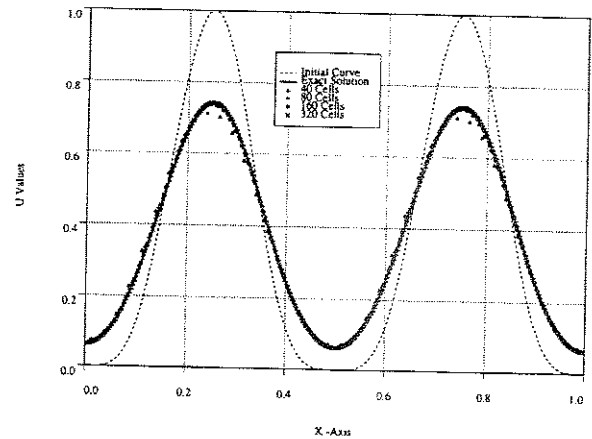


FIGURE 4 Advection-Diffusion Case with MUSCL limiter and BGK solver ($Re = 400$).

Case (2) Shock Tube Problems

Two standard shock tube problems are chosen. The Sod case is a Riemann problem for the one dimensional Euler equations and is taken from reference [31]. The density distribution computed using 100 cells is shown in Figure (6) and compared with the exact solution which is plotted as a solid line. The Lax-Harten case is also a Riemann problem for the

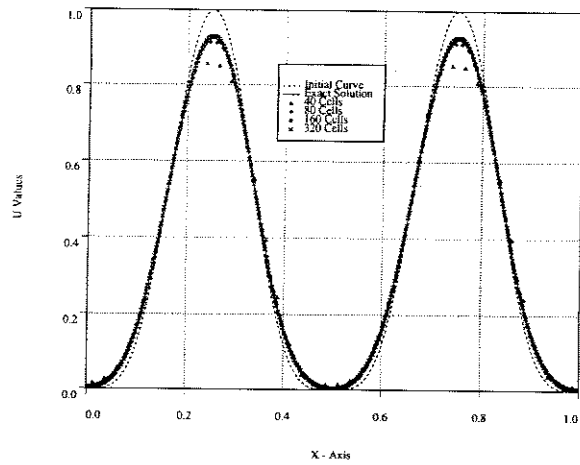


FIGURE 5 Advection-Diffusion Case with MUSCL limiter and BGK Solver ($Re = 2000$).

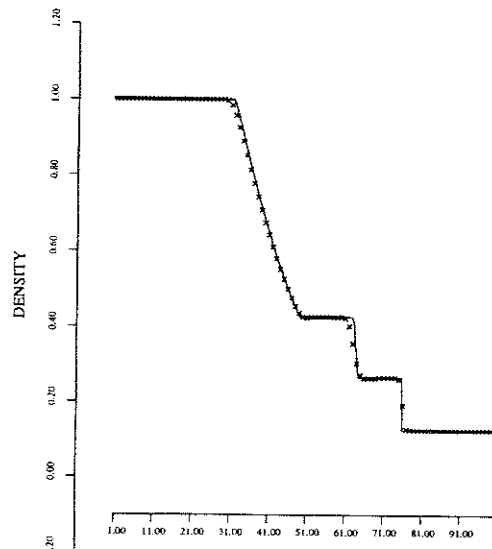


FIGURE 6 Sod case with MUSCL limiter and BGK Solver (100 cells).

Euler equations [30]. The density distribution computed using 100 cells is shown in Figure (7). The accuracy of the computed results are comparable to that obtained with higher order ENO schemes by other authors [8, 30], although a MUSCL limiter is used in reconstruction step of the BGK-type scheme.

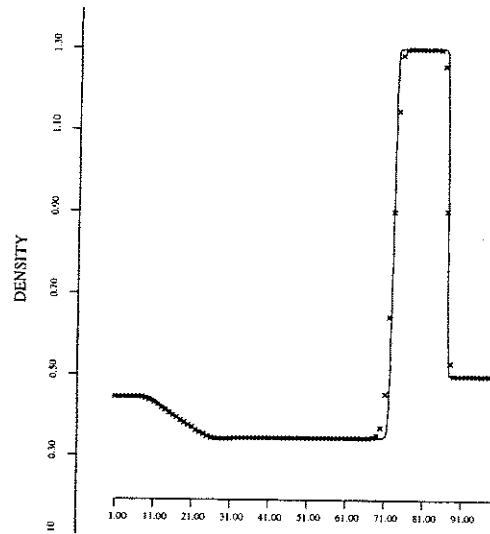


FIGURE 7 Lax-Harten case with MUSCL limiter and BGK Solver (100 cells).

Case(3)Blast Wave Problem

The blast wave problem, first proposed by Woodward and Colella [33], requires the computation of a head-on collision between two blast waves and the resulting series of shocks and contact discontinuities. The density distribution computed with the MUSCL limiter and the BGK flux function using 400 cells is shown by the symbols in Figure (8). The solid line is obtained with the same scheme and 800 cells. From the results, we can see that the shock and contact discontinuity waves are well resolved.

It is well known that several existing schemes, such as the PPM method, need to be augmented by a steepening technique in order to improve the accuracy of the results for this test case. Thus, we have also investigated the use of steepening techniques in the reconstruction stage of the BGK-type method. The density distribution computed using 400 cells and Huynh's third-order interpolation [10] scheme with sharpening of the contact discontinuity coupled with our BGK-type flow solver is shown in Figure (9). This result, which was obtained using a $\kappa = 10$, compares extremely well with the solid line which is again the fine grid solution of Figure (8). However, as in the case with other

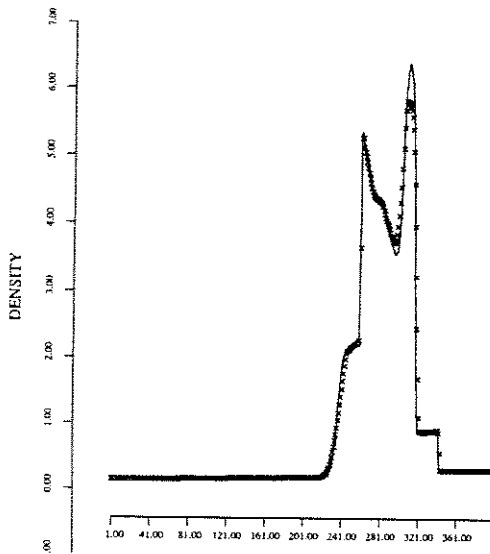


FIGURE 8 Blast-Wave case with MUSCL limiter and BGK Solver (400 cells).

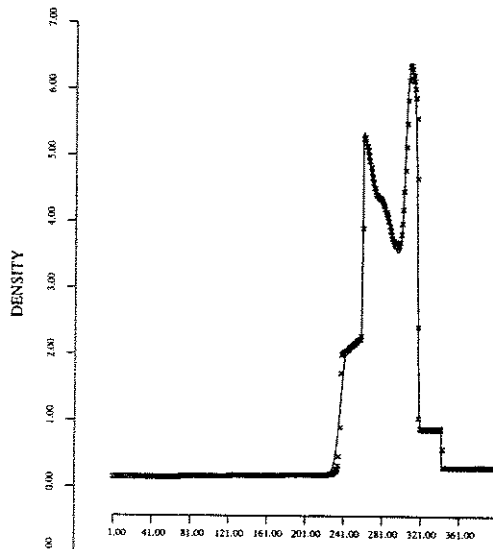


FIGURE 9 Blast-wave case with Huynh's limiter and BGK Solver (400 cells).

schemes, it is observed that steepening techniques reduce the robustness of our numerical method.

Case (4) Shu-Osher Problem

The Shu-Osher test case requires the calculation of a moving shock at Mach number 3 interacting with

sine waves. As observed by Shu and Osher [30], MUSCL type TVD schemes produce very smeared results for the density distributions. Figure (10) and Figure (11) show the density distributions computed on a mesh with 400 cells using the BGK solver coupled, respectively, with a MUSCL and a 4th-order ENO [8] interpolation of the pointwise values at the cell interface. The results confirm that an accurate calculation of this test case requires higher order reconstructions.

Case (5) Forward Facing Step with Mach 3

The forward-facing step test is carried out on a uniform mesh with 240×80 cells. The computed density and pressure distributions are presented in Figure (12). Notice that the BGK-type scheme does not require any special treatment at the corner, and does not produce any expansion shocks at the corner.

Case (6) Double Mach Reflection

The double Mach reflection problem is calculated on a computational domain with 360×120 cells.

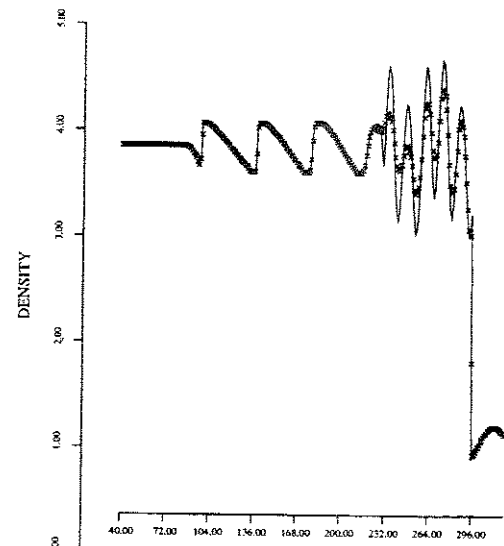


FIGURE 10 Shu-Osher case with MUSCL limiter and BGK Solver (400 cells).

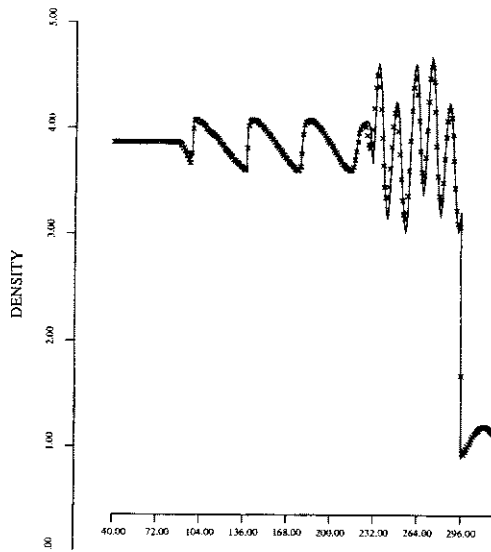


FIGURE 11 Shu-Osher case with 4th-order ENO Limiter and BGK Solver.

The problem is set up by driving a strong shock down a tube which contains a wedge. The computed density and pressure distributions after the collision between the shock and the wedge are shown on Figure (13). The carbuncle phenomenon reported in

reference [14] was never observed with our BGK-type scheme.

Case(7) An Impulsively Started Cylinder

Strong shocks, and expansions as well as subsonic flow regions are presented in both steady and unsteady hypersonic flows induced by the impulsive start of a cylinder. A monotonic numerical scheme is needed to capture, crisply and without spurious oscillations, the abrupt change of flow variables across a shock wave. Moreover, a numerical scheme should be capable of maintaining positivity of the flow variables, to avoid the occurrence of unphysical negative values for quantities such as pressure and/or temperature in regions of low density and low temperatures created by extreme expansions. In the present paper initial Mach numbers of $M = 2.5, 3.5$ were chosen as test cases of hypersonic flows which present all the flow features discussed above. This problem imposes a particular difficulty not only for unsteady but also for steady flow computations because the very high expansion in the rear part of the cylinder produces a vacuum-like low pressure and low density region.

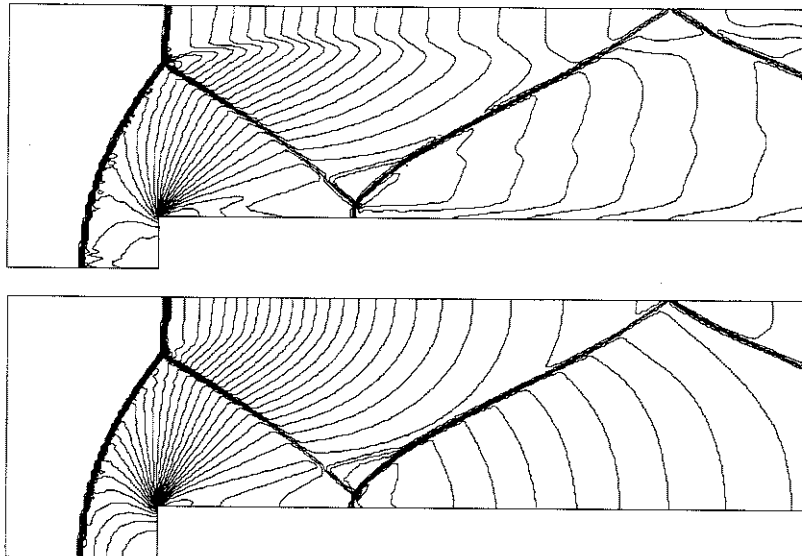


FIGURE 12 Density and Pressure Distributions from the Splitting BGK-type Scheme with MUSCL limiter.

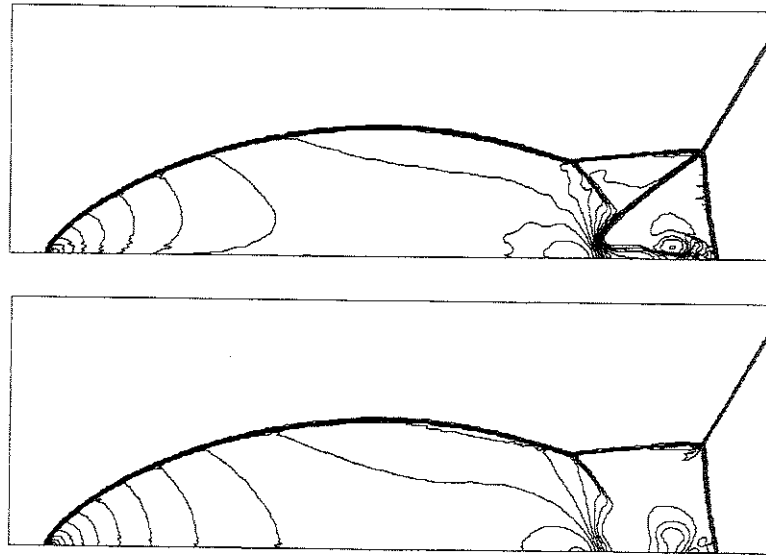


FIGURE 13 Density and Pressure Distributions from the Splitting BGK-type Scheme with MUSCL Limiter.

If the kinetic energy is so large that the difference between the total energy and the kinetic energy is in the range of round-off error, one should limit the lower bound of the difference with the order of round-off to avoid meaningless computations. This problem is solely caused by the finite precision of the hardware and not by the numerical scheme. The round-off error is usually of the order $O(10^{-12}) \sim O(10^{-16})$. The present computations were performed using a Silicon Graphics INDIGO 2 workstation with an observed round-off error of order $O(10^{-18})$. Thus a lower bound of 10^{-16} was selected. Several numerical schemes described in reference [14] have been applied to this problem.

All of the schemes have severe difficulties in maintaining positive pressure and/or density, and generally need *ad hoc* fixes. Most of the second-order schemes simply fail. Our BGK-type scheme, however, does not seem to have particular difficulties in preserving positivity during the whole time integration. This finding is verified for both first and second-order schemes.

Two different grids with 90×25 , and 180×50 cells were used. The coarse grid is shown in Figure (14). The grid distribution is uniform in the angular direction (90 or 180 cells) while the cells in

the radial direction grid (25 or 50 cells) are slightly clustered to the surface. The ratio of inner radius to outer radius is 10, and all the calculations were carried out using a CFL of 0.5. Figure (15) and Figure (16) show the computed density, pressure and Mach number distributions along the symmetry line and the upper surface of the cylinder at times

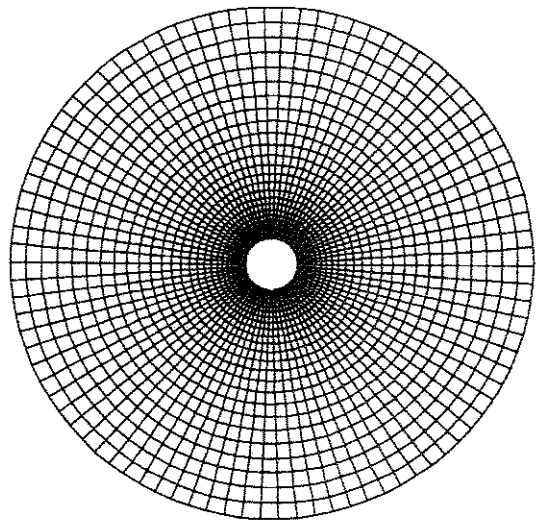


FIGURE 14 Grid Distribution around the Cylinder (90×25 cells).

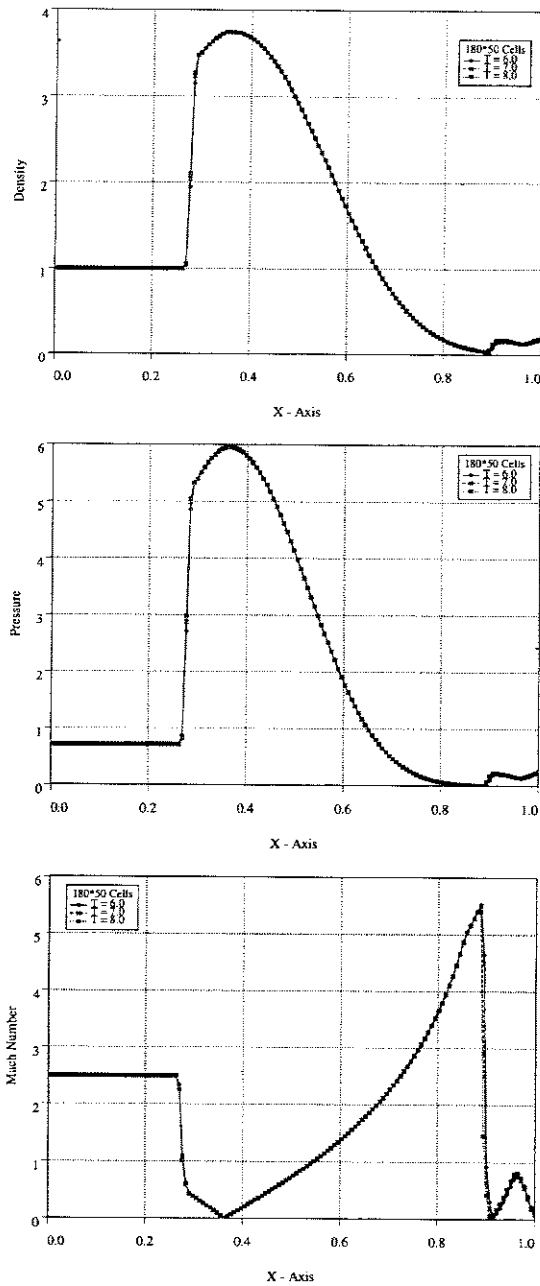


FIGURE 15 Density, Pressure and Mach Number Distributions for $M = 2.5$.

of $T=6.0, 7.0, 8.0$ corresponding to a free stream Mach number of $M = 2.5, 3.5$ respectively. It can be seen that the results at three different times practically collapse to a single curve. This indicates that

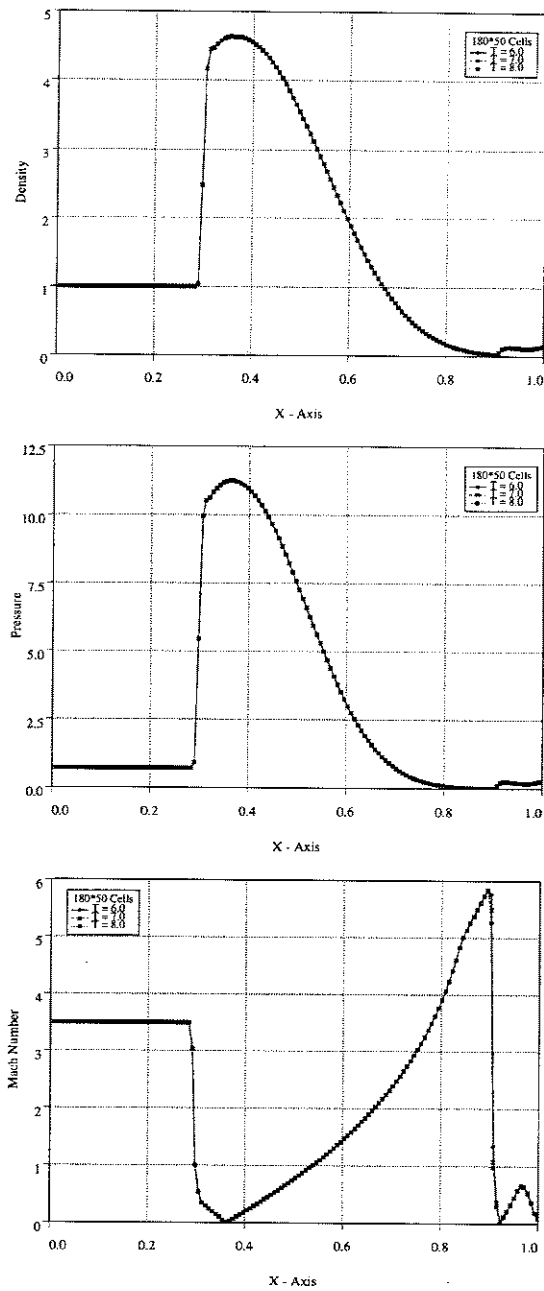
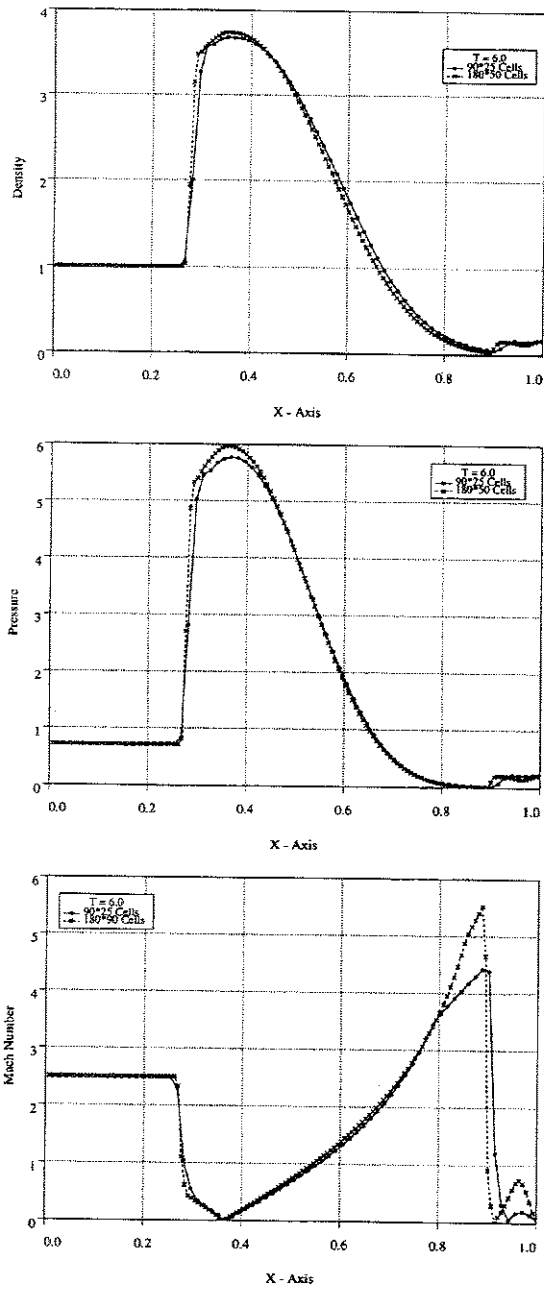
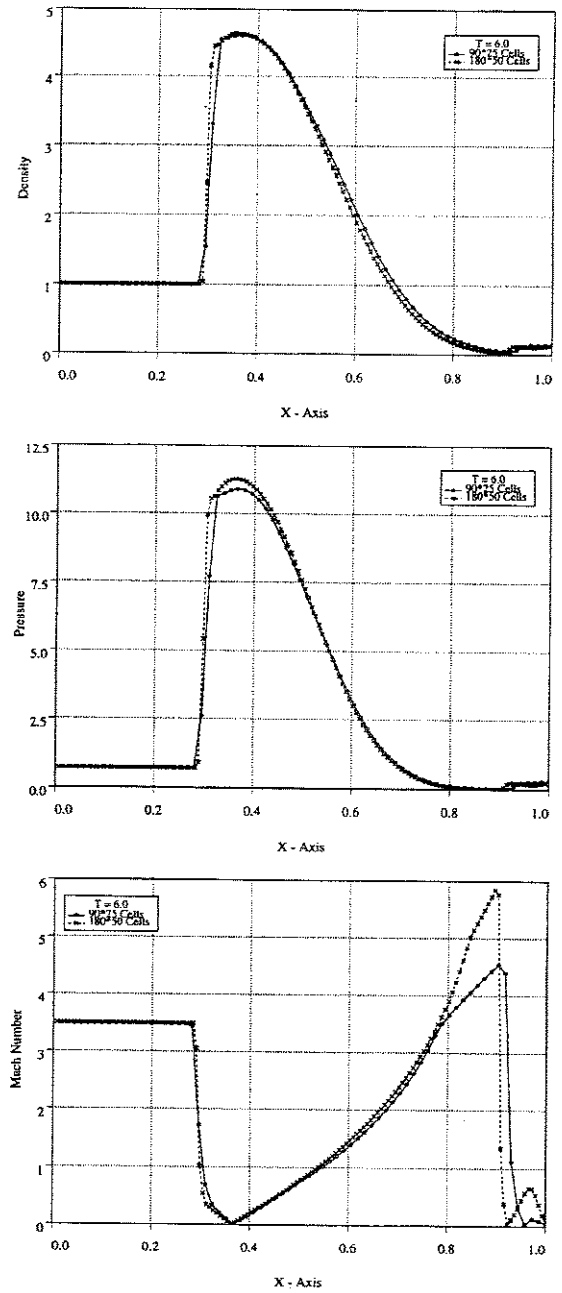


FIGURE 16 Density, Pressure and Mach Number Distributions for $M = 3.5$.

the computed results at $T=6.0$ have reached a steady state. Figure (17) and Figure (18) show the density, pressure and Mach number distributions at $T=6.0$. Notice that the bow shock wave is captured

FIGURE 17 Grid Refinement Study for $M = 2.5$.FIGURE 18 Grid Refinement Study for $M = 3.5$.

with two interior points. Also, on the finer grid, the shock profile is sharper and the expansion in the rear part of cylinder is more extreme, leading to a higher Mach number. Our results show a much

higher Mach number than the result in reference [18] even on a coarser grid. This again indicates that BGK-type schemes may yield a less diffusive solution with a consequent higher accuracy.

Figure (19) and Figure (20) show the density, pressure and Mach contours for $M = 2.5, 3.5$. Forty contour levels, equally spaced from the maximum and minimum values, are used. Both the bow shock and the V-shape shock induced from the expansion are captured very well with a relatively coarse grid.

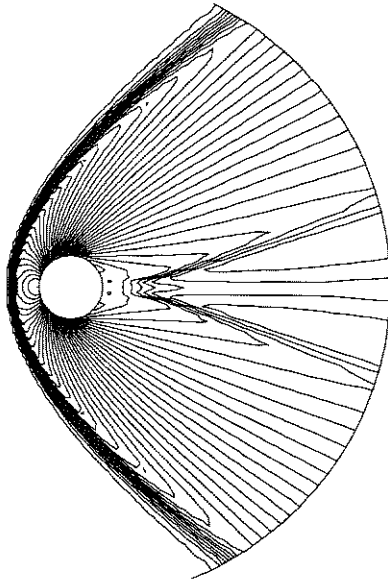


FIGURE 19a (Density Contours).

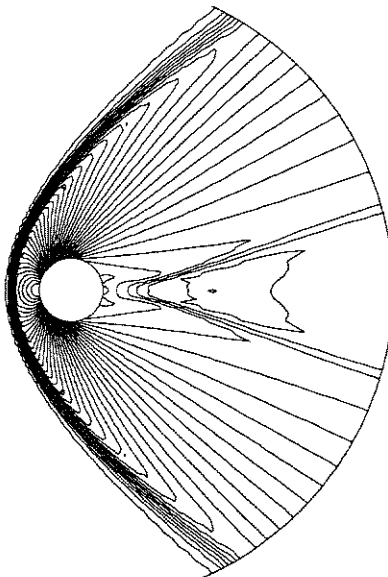
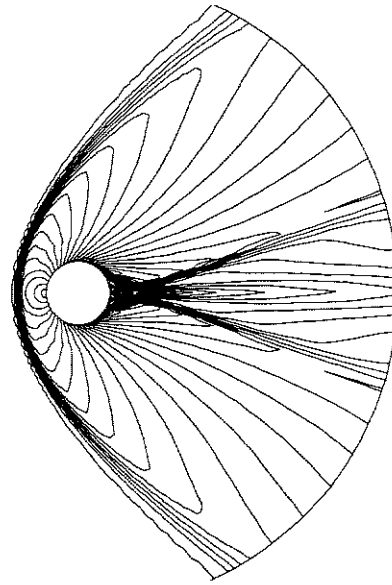


FIGURE 19b (Pressure Contours).



(c)

FIGURE 19 Density, Pressure and Mach Contours for $M = 2.5$.

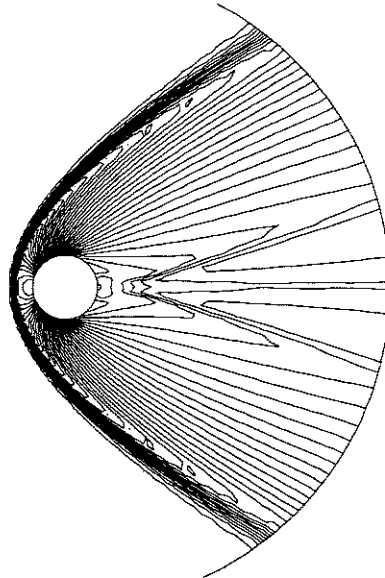


FIGURE 20a (Density Contours).

4. CONCLUSION

Both the initial reconstruction stage and the gas evolution stage can affect the accuracy and robustness of a numerical scheme. While the reconstruc-

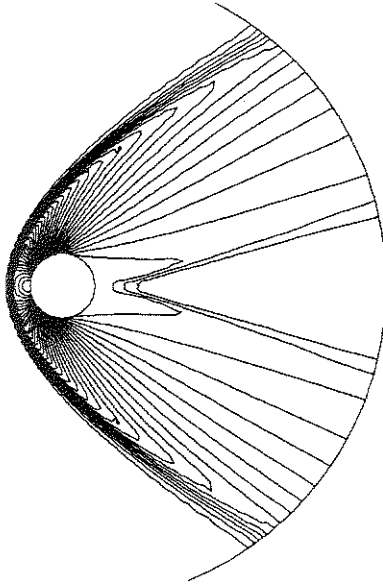
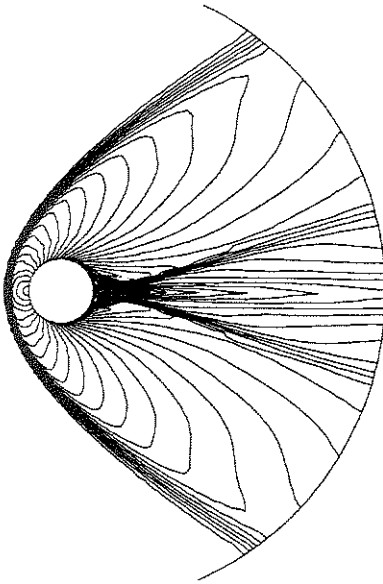


FIGURE 20b (Pressure Contours).



(c)

FIGURE 20 Density, Pressure and Mach Contours for $M = 3.5$.

tion step is mainly a numerical artifact, the dynamical evolution step should model the physics of the flow as accurately as possible. The BGK-type schemes provide an alternative and advanced gas

evolution model, which has many advantages over Godunov-type schemes. The initial condition in the reconstruction step is more flexible and the final gas distribution function yields the Navier-Stokes equations. The physical evolution for the BGK-type schemes is based on the simple fact that a nonequilibrium state will approach an equilibrium state in both space and time due to particle collisions. This process is accompanied by an increase of entropy. Also, the BGK-type schemes eliminate some of the difficulties encountered by multidimensional upwind schemes and satisfy the positivity condition. Following earlier papers [23, 35, 36, 13, 37], the present paper shows the progressive development of the BGK-type schemes. The comprehensive numerical results presented in this paper validate both the physical and numerical considerations used in the development, and indicate the level of maturity reached by this class of schemes.

Acknowledgments

The research in this paper is supported by Grant URI/AFOSR F49620-93-1-0427 for all authors.

APPENDIX A

Linear Advection-Diffusion Equation:

The linear advection-diffusion equation in one-dimension is written as

$$U_t + cU_x = vU_{xx},$$

where v is the viscosity coefficient. The above equation can be derived from the BGK model

$$f_t + uf_x = (g - f)/\tau,$$

assuming that

$$g = U \left(\frac{\lambda}{\pi} \right)^{1/2} e^{-\lambda(u-c)^2},$$

together with the conservation constraint

$$\int (f - g) d\Xi = 0.$$

The Chapman-Enskog expansion of the BGK model gives

$$f = g - \tau(g_t + ug_x). \quad (15)$$

The corresponding advection-diffusion equation

$$U_t + cU_x = \frac{\tau}{2\lambda} U_{xx} - \frac{3\tau^3}{4\lambda^2} U_{xxxx}$$

is obtained by substituting Eq. (15) into the relation $\int (f_t + uf_x) du = 0$ obtained from the conservation constraint, and by integrating in the particle velocity space. The 4th-order derivative in the above equation has the very nice property of stabilizing the numerical scheme [9]. Thus, if we take $\tau = 2v\lambda$, the advection-diffusion equation is recovered from the BGK model.

The numerical scheme for the linear advection-diffusion equation can be obtained from the scheme presented in this paper by following several simplifications:

1. Make the number of the internal degrees of freedom $K = 0$.
2. Only keep the first moment of ψ_x with $\psi = 1$.
3. Both f and g have the same λ , which is chosen initially, for example $\lambda = 1$. The collision time τ is determined afterwards by $\tau = 2\lambda v$, where v is known.

APPENDIX B

Moments of the Maxwellian Distribution Function: In the gas-kinetic scheme, we need to evaluate moments of the Maxwellian distribution function with bounded and unbounded integration limits. Here, we list some general formulas.

Firstly, we assume that the Maxwellian distribution for one dimensional flow is

$$g = \rho \left(\frac{\lambda}{\pi} \right)^{(k+1)/2} e^{-\lambda((u-U)^2 + \xi^2)},$$

where ξ has K degrees of freedom. Then, by introducing the following notation for the moments of g ,

$$\rho \langle \dots \rangle = \int (\dots) g du d\xi,$$

the general moment formula becomes

$$\langle u^n \xi^l \rangle = \langle u^n \rangle \langle \xi^l \rangle,$$

where n is an integer, and l is an even integer (owing to the symmetrical property of ξ). The moments of $\langle \xi^l \rangle$ are:

$$\langle \xi^2 \rangle = \left(\frac{K}{2\lambda} \right)$$

$$\langle \xi^4 \rangle = \left(\frac{3K}{4\lambda^2} + \frac{K(K-1)}{4\lambda^2} \right).$$

The values of $\langle u^n \rangle$ depend on the integration limits. If the limits are from $-\infty$ to $+\infty$, we have

$$\langle u^0 \rangle = 1$$

$$\langle u \rangle = U$$

$$\langle u^{n+2} \rangle = U \langle u^{n+1} \rangle + \frac{n+1}{2\lambda} \langle u^n \rangle$$

When the integral is from 0 to $+\infty$ as $\langle \dots \rangle_{>0}$, the error function and the complementary error function, appear in the formulation. Thus, the moments for u^n in the half space are,

$$\langle u^0 \rangle_{>0} = \frac{1}{2} \operatorname{erfc}(-\sqrt{\lambda}U)$$

$$\langle u^1 \rangle_{>0} = U \langle u^0 \rangle_{>0} + \frac{1}{2} \frac{e^{-\lambda U^2}}{\sqrt{\pi \lambda}}$$

$$\langle u^{n+2} \rangle_{>0} = U \langle u^{n+1} \rangle_{>0} + \frac{n+1}{2\lambda} \langle u^n \rangle_{>0}$$

Similarly,

$$\langle u^0 \rangle_{<0} = \frac{1}{2} \operatorname{erfc}(\sqrt{\lambda} U)$$

$$\langle u^1 \rangle_{<0} = U \langle u^0 \rangle_{<0} - \frac{1}{2} \frac{e^{-\lambda U^2}}{\sqrt{\pi \lambda}}$$

$$\langle u^{n+2} \rangle_{<0} = U \langle u^{n+1} \rangle_{<0} + \frac{n+1}{2\lambda} \langle u^n \rangle_{<0}$$

References

- [1] Bhatnagar, P. L., Gross, E. P. and Krook, M. (1954). "A model for Collision Processes in Gases I: Small Amplitude Processes in Charged and Neutral One-Component Systems", *Phys. Rev.*, **94**, 511–525.
- [2] Chiu, C. and Zhong, X. (1995). "Simulation of Transient Hypersonic Flow Using the ENO Schemes", AIAA-95-0469, 33rd Aerospace Sciences Meeting and Exhibit.
- [3] Deshpande, S. M. (1986). "A Second Order Accurate, Kinetic-Theory Based, Method for Inviscid Compressible Flows", NASA Langley Tech. paper No. 2613.
- [4] Einfeldt, B., Munz, C. D., Roe, P. L. and Sjögren, B. (1991). "On Godunov-type Methods near Low Density", *J. Comput. phys.*, **92**, 273.
- [5] Eppard, W. and Grossman, B. (1993). "A multidimensional kinetic-based upwind solver for the Euler equations", AIAA 11th CFD Conference, Orlando, FL.
- [6] Godunov, S. K. (1959). "A Difference Scheme for Numerical Computation of Discontinuous Solutions of Hydrodynamic Equations", *Math. Sbornik*, **47**, 271.
- [7] Harten, A. (1984). "On a Class of High Resolution Total Variation Stable Finite Difference Schemes", *SIAM J. Numer. Anal.*, **21**, 1–23.
- [8] Harten, A., Engquist, B., Osher, S. and Chakravarthy, S. (1987). "Uniformly High Order Accurate Essentially Non-Oscillatory Schemes, III", *J. Comput. Phys.*, **71**, 231–303.
- [9] Hirsch, C. (1990). "The Numerical Computation of Internal and External Flows", John Wiley and Sons, Vol. 1 and 2.
- [10] Huynh, H. T. (1995). "Accurate Upwind Methods for the Euler Equations", *SIAM J. Numer. Anal.*, **32** (5), 1565–1619.
- [11] Jameson, A. (1995). "Positive Schemes and Shock Modeling for Compressible Flows", *Int. J. Num. Met. in Fluids*, **20**, 743–776.
- [12] Jin, S. and Xin, Z. P. (1995). "The Relaxation Schemes for Systems of Conservation Laws in Arbitrary Space Dimension", *Commun. Pure Appl. Math.*, **48**, 235.
- [13] Kim, C. A., Xu, K., Martinelli, L. and Jameson, A. (1995). "Analysis and Implementation of the Gas-kinetic BGK Scheme for Computational Gas Dynamics", accepted by *Int. J. Num. Met. in Fluids*, Nov., 1995.
- [14] Kim, C. A. and Jameson, A. (1995). "Flux Limited Dissipation Schemes for High Speed Unsteady Flows" AIAA 95-1738, 12th AIAA CFD Conference.
- [15] Kogan, M. N. (1969). "Rarefied Gas Dynamics", Plenum Press, New York.
- [16] Lax, P. D. (1972). "Hyperbolic Systems of Conservation Laws and the Mathematical Theory of Shock waves", in *Regional Conference Series Lecture in Applied Math*, Vol. 11 (SIAM, Philadelphia).
- [17] Levermore, C. D. (1995). "Moments Closure Hierarchies for Kinetic Theory", submitted to *J. of Statistical Physics*.
- [18] Lyra, P. R. M., Morgan, K., Peraire, J. and Peiro, J. (1994). "TVD Algorithms for the Solution of the Compressible Euler Equations on Unstructured Meshes", *Int. J. for Num. Met. in Fluids*, **19**, 827–847.
- [19] Macrossan, M. N. (1989). "The Equilibrium Flux Method for the Calculation of Flows with Non-Equilibrium Chemical Reactions", *J. of Comput. Phys.*, **80**, 204–231.
- [20] Macrossan, M. N. and Oliver, R. I. (1993). "A Kinetic Theory Solution Method for Navier-Stokes Equations", *Int. J. for Num. Met. in Fluids*, **17**, 177.
- [21] Mandal, J. C. and Deshpande, S. M. (1994). "Kinetic Flux Vector Splitting for Euler Equations", *Computers and Fluids*, **23** (2) 447.
- [22] Perthame, B. (1992). "Second-Order Boltzmann schemes for compressible Euler equation in one and two space dimensions", *SIAM J. Numer. Anal.*, **29** (1).
- [23] Prendergast, K. H. and Xu, K. (1993). "Numerical Hydrodynamics from Gas-Kinetic Theory" *J. of Comput. Phys.*, **109**, 53.
- [24] Pullin, D. I. (1980). "Direct Simulation Methods for Compressible Inviscid Ideal Gas Flow", *J. of Comput. Phys.*, **34**, 231–244.
- [25] Quirk, J. (1994). "A Contribution to the Great Riemann Solver Debate", *Int. J. Num. Met. in Fluids*, **18** (6).
- [26] Reitz, R. D. (1981). "One-Dimensional Compressible Gas Dynamics Calculations Using the Boltzmann Equations", *J. of Comput. Phys.*, **42**, 108–123.
- [27] Roe, P. L. (1981). "Approximate Riemann Solvers, Parameter Vectors and Difference Schemes", *J. Comput. Phys.*, **43**, 357.
- [28] Roe, P. L. (1986). "Characteristic-based schemes for the Euler equations", *Ann. Rev. Fluid Mech.*, **18**, 337.
- [29] Sanders, R. H. and Prendergast, K. H. (1974). "The possible relation of the three-kiloparsec arm to explosions in the galactic nucleus," in *Astrophysical Journal*, **188**.
- [30] Shu, C. W. and Osher, S. (1989). "Efficient Implementation of Essentially Non-Oscillatory Shock-Capturing Schemes II", *J. Comput. Phys.*, **83**, 32–78.
- [31] Sod, G. A. (1978). "A Survey of Several Finite Difference Methods for System of Nonlinear Hyperbolic Conservation Laws", *J. Comput. Phys.*, **27**, 1–31.
- [32] van Leer, B. (1977). "Towards the Ultimate Conservative Difference Scheme IV, A New Approach to Numerical Convection", *J. Comput. Phys.*, **23**, 276.
- [33] Woodward, P. and Colella, P. (1984). "Numerical Simulations of Two-dimensional Fluid Flow with Strong Shocks", *J. Comput. Phys.*, **54**, 115.

- [34] Xu, K. (1993). "Numerical Hydrodynamics from Gas-Kinetic Theory", Ph.D. thesis, Columbia University.
- [35] Xu, K. and Prendergast, K. H. (1994). "Numerical Navier-Stokes Solutions from Gas-Kinetic Theory", *J. Comput. Phys.*, **114**, 9–17.
- [36] Xu, K., Martinelli, L. and Jameson, A. (1995). "Gas-Kinetic Finite Volume Methods, Flux-Vector Splitting and Artificial Diffusion", *J. Comput. Phys.*, **120**, 48–65.
- [37] Xu, K. and Jameson, A. (1995). "Gas-Kinetic Relaxation (BGK-Type) Schemes for the Compressible Euler Equations", AIAA 95–1736, 12th AIAA CFD conference.